CAAP Quarterly Report

[06/27/2025]

Project Name: "All-in-One Multifunctional Cured-In-Place Structural Liner for Rehabilitating of Aging Cast Iron Pipelines"

Contract Number: 693JK32250009CAAP

Prime University: North Dakota State University

Prepared By: [Ying Huang, ying.huang@ndsu.edu, 701-231-7651]

Reporting Period: [03/27/2025– 06/27/2025]

Project Activities for Reporting Period:

In the last reporting period (10th quarterly report), Tasks 2, 3, 4, and 5 were carried out as proposed. During the current reporting period (the 11th quarterly report), the research team has a delay in some of the tasks and made a no-cost extension request in May 2025 and is pending for review and approval. While at the same time, the team has continued making steady progress on the selected tasks. Key activities accomplished during this quarter are summarized in this report.

Task 2.1 Preparation of Vitrimer Epoxy Resins, Characterization, and Optimization of Processing and Curing Conditions (97%): During the past quarter, the research team (Dr. Long Jiang and Austin Knight, Ph.D. student at NDSU) investigated approaches to improve catalyst dissolution and optimized the resin formulations to enhance the thermal performance of the self-healing polymers. It was determined that a mixture of acrylate and methacrylate reactive diluents produced thermoplastics with the lowest relaxation temperature. To address the melting behavior typically observed in homopolymers, an acrylate reactive diluent containing sufficient diacrylate impurities was used, forming a new formulation. The formulation is expected to offer improved thermal characteristics; which was tested in this study, and its dilatometry results are presented in the following section. Key findings are summarized below:

(1) Acrylate Monomer for Dissolving the Transesterification Catalyst: An additional acrylate reactive diluent (RDA2) was procured to aid TEC dissolution and reduce UV-curing inhibition. Though RDA2 did not fully dissolve TEC at typical concentrations, it was tested as an RDA substitute. Dilatometry on a DFA formulation with a 50:50 mix of RDA2 and RDMA (with 20 parts TEC) was compared to RDMA and RDA:RDMA blends (Figure 1(a)). RDA lowered Tg below room temperature, had little effect on Tv, and reduced strain. RDA2 also lowered Tg but increased strain. The RDA2 sample fractured at 122.25°C after an unclear transition, prompting further tests with varied RDA2 concentrations under lower stress. At 10 parts RDA2, both Tg and Tv decreased, and strain rose. At 50 and 90 parts, the curve structure changed and Tv became undefined (Figure 1(b)). High strain at room temperature suggests Tg is below room temperature, and the elastic plateau at high temperatures points to diacrylate impurities in RDA2. Since the target Tg is 70–90°C, future formulations should limit acrylate content to ~10 parts to maintain rigidity.

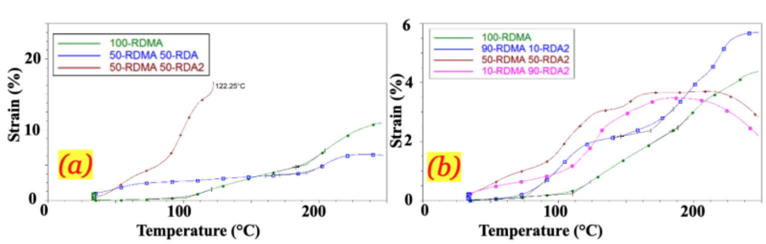

Figure 1. The dilatometry results for new DFA formulations (a) tested at 100 kPA and (b) tested at 10 kPa.

(2) Aromatic Adduct Crosslinkers: The previously used crosslinker (DFA) is a short aromatic compound. To improve vitrimer properties, its length was increased by adducting multiple aromatic units, resulting in new crosslinkers named DFAAr, DFAAr2, and DFAAr3, where the number indicates the number of aromatic units. Longer crosslinkers offer more flexibility and additional transesterification sites, enhancing vitrimer behavior. Formulations using 100 parts RDMA and 20 parts TEC were tested via dilatometry (Figure 2). Tg decreased from DFAAr to DFAAr2, with little change between DFAAr2 and DFAAr3. A similar pattern was observed for Tv. Maximum strain peaked with DFAAr2 but dropped significantly for DFAAr3. This reduction is likely due to the increased concentration of rigid aromatic groups, which, while enabling more transesterification sites, also increase rigidity and limit vitrimer reactions.

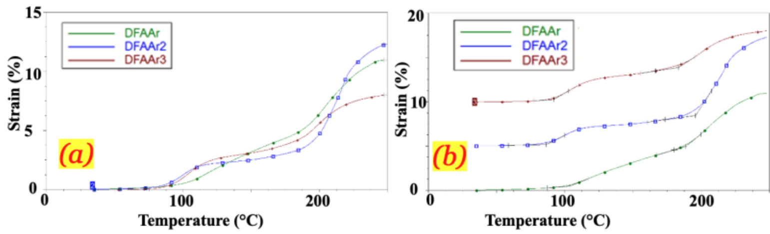

Figure 2. The dilatometry results for (a) the DFAAr, DFAAr2, DFAAr3 formulations and (b) the same results but offset in strain by 5%.

(3) Aliphatic Adduct Crosslinkers: Aromatic groups in crosslinkers are bulky and restrict chain mobility, making adhesives more rigid and potentially limiting vitrimer reactions. To explore alternatives, aliphatic units were used to create crosslinkers named DFAAl, DFAAl2, and DFAAl3, where higher numbers indicate longer chains. So far, only DFAAl has been synthesized. A formulation with 100 parts RDMA and 20 parts TEC was tested via dilatometry and compared to its aromatic counterpart (DFAAr) (Figure 3). While Tg and Tv were similar, the DFAAl formulation showed significantly higher strain, indicating better flowability when heated—an advantage for self-healing and vitrimer behavior. Based on trends observed with aromatic crosslinkers, longer aliphatic chains are expected to further reduce Tg and Tv, making this system promising for enhancing vitrimer properties.

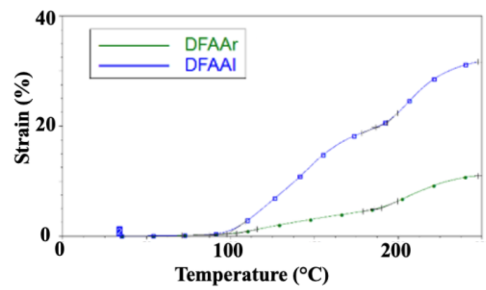

Figure 3. The dilatometry results for the DFAAr and DFAAl formulations with 100 parts DFMA and 20 parts TEC.

Task 3.3 Reducing the Permeability and Investigating the Interfacial Bonding Chemical Analysis (85%): In previous work, the research team (Dr. Liangliang Huang and Hao Yuan, Ph.D. student at the University of Oklahoma) performed targeted optimizations for the vitrimer systems. During the current reporting period, a comprehensive evaluation of the previously developed vitrimer model was carried out, with a focus on assessing its glass transition temperature, porosity, and mechanical properties.

(1) Glass Transition Temperature: To determine the appropriate simulation temperature, two critical transition temperatures associated with the viscoelastic behavior of vitrimers must be considered: the glass transition temperature (Tg) and the topology freezing temperature (Tv). Tg represents the temperature range over which the material transitions from a glassy to a rubbery state, a characteristic common to all polymeric materials. In contrast, Tv is a distinctive characteristic of vitrimers, defined as the temperature at which

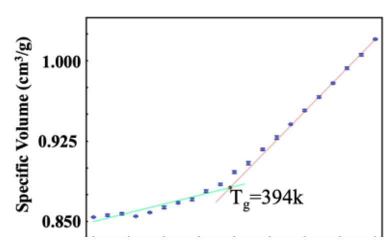

Figure 4. Specific volume vs. glass transition temperature.

the timescale of bond exchange reactions (BER) becomes shorter than the timescale of material deformation. This facilitates the rearrangement of the network topology, enabling material flow. Notably, visible self-healing occurs at temperatures above both Tg and Tv, as both network topology rearrangement and segmental motion are prerequisites for the self-healing process. Therefore, the temperature for self-healing simulations should be carefully selected based on Tg. The Tg was determined using the heating-up method. Initially, as presented in Figure 4, the MD model was equilibrated at 200 K, followed by a gradual increase in temperature up to 600 K. At each 20 K interval, the temperature was maintained for 10 ns, with the data from the subsequent 1 ns utilized for analysis to ensure the attainment of a stable specific volume at each temperature point. Tg was identified as the intersection of two linear regression lines, corresponding to the glassy phase (200–400 K) and the rubbery phase (500–600 K). The calculated Tg from this is about 394 K, which is very close to the experimentally determined value (410 K).

(2) Porosity: As shown in Figure 5, the porosity of the vitrimer at 300 K is 35.38%. With increasing temperature, the porosity increases to 37.85% at 400 K and further to 41.95% at 500 K. Additionally, the structural snapshots indicate that at 300 K, most voids remain isolated, whereas at higher temperatures, many voids merge to form interconnected networks. However, the impact of these voids on gas transport has not yet been analyzed. To comprehensively assess their influence on gas transmission, an aperture analysis of each individual void is necessary.

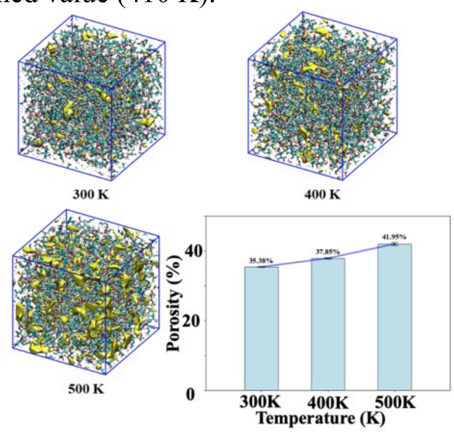

Figure 5. Void structures in the vitrimer model at different temperatures and illustrating the variation of porosity as a function of temperature.

(3) Mechanical Property: The mechanical properties of the vitrimer system were characterized through tensile stress–strain simulations, and the corresponding Young's modulus was calculated. The results in Figure 6 show that in the absence of ester exchange reactions, the Young's modulus is 2.15 GPa at 300 K and decreases to 1.20 GPa at 400 K, indicating a reduction in mechanical strength with increasing temperature. However, when ester exchange reactions are enabled at 400 K, the Young's modulus significantly increases to 3.04 GPa, surpassing the system without the exchange reaction under the same conditions. Additionally, comparison with the experimentally measured Young's modulus at room temperature (4.43 GPa) reveals that all simulated values are within the same order of magnitude, thereby supporting the validity and predictive capability of the model.

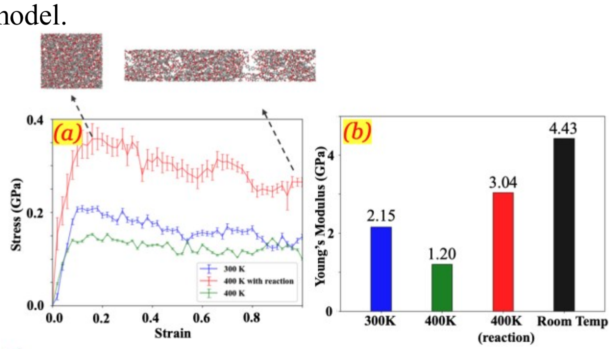

Figure 6. (a) Stress–strain curve for the first simulation test; (b) comparison of Young's modulus for systems under different temperatures and conditions, with and without the ester exchange reaction, alongside corresponding experimental values.

Task 3.4 Finite Element Numerical Analysis to Guide the Design of the Developed High-performance Healable CIPP Structural Liner (93%): During this reporting period, the research team (Dr. Chengcheng Tao, Junyi Duan, Ph.D. student from Purdue University) have conducted finite element analysis (FEA) on pitting corrosion in cast-iron pipes rehabilitated by liners as summarized below:

(1) Finite element analysis on pitting corrosion in cast-iron pipes rehabilitated by liners: A three-dimensional finite element model is developed to simulate the mechanical behavior of pitting-corroded cast-iron pipelines under internal pressure, as shown in Figure 7. The pipeline is modeled as a 2400 mm-long hollow cylinder with inner and outer diameters of 150 mm and 165 mm, respectively. Cast iron is assumed to be linear elastic, with a Young's modulus of 100 GPa and Poisson's ratio of 0.3, due to its higher stiffness compared to the adhesive layer and CIPP liner. A uniform internal pressure of 1.5 MPa is applied to the inner surface of the CIPP liner to simulate gas transmission conditions. Boundary effects are minimized by constraining both ends of the pipe against movement and rotation. The three-layer structure is modeled with Coulomb's law to define interfacial interactions. Two contact pairs, pipe to adhesive and adhesive to liner, are modeled using a friction coefficient of 0.3 tangentially and hard contact normally. Pitting corrosion is simulated using semi-spherical or semi-ellipsoidal geometries at the mid-top surface of the pipe, with variations in pit depth and shape ratio.

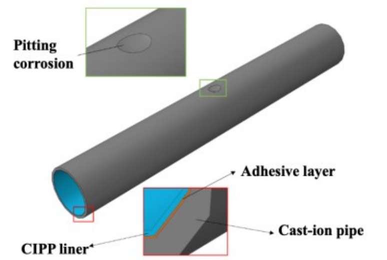

Figure 7. FEA model of pitting corroded cast iron pipe with liner.

(2) Effect of pit depth: The depth of pitting corrosion serves as a critical parameter for evaluating the severity of external corrosion and its impact on the structural integrity of cast-iron pipes. Figure 8(a) illustrates the maximum tensile stress on the pipe under various pit depths. At a pit depth of 5 mm, the maximum stress is 30.48 MPa, a level that does not pose a significant threat to the pipe system. When the depth increases to 10 mm, the stress increases moderately to 40.38 MPa. However, at a pit depth of 15 mm, just before perforation, the maximum tensile stress surges to 77.14 MPa. This nonlinear increase in tensile stress as the pit depth grows highlights the significant damage caused by corrosion. While stress levels at 15 mm depth do not result in immediate failure of the cast-iron pipe, the sharp surge in stress highlights the rapid structural deterioration and potential failure.

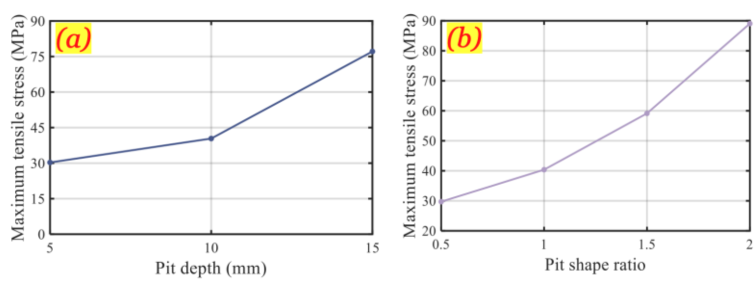

Figure 8. The maximum tensile stress on pipes with (a) different pit depths, and (b) different pit shape ratios.

(3) Effect of pit shape ratio: In addition to the typical circular pit on cast iron pipelines, we computationally assess irregular pit, such as semi-ellipsoidal corrosion pit. The pit width is defined as the dimension along the circumferential direction of the pipe, and the pit length is the dimension along the longitudinal direction of the pipe. We set the pit shape ratio as the pit length divided by pit width. The pit depth is fixed as 10 mm in this study, and four pit shape ratios are considered: 0.5, 1, 1.5, and 2. Figure 8(b) shows that the maximum tensile stress on the pipe increases with the pit shape ratio, with an approximately 300% increase from a pit shape ratio of 0.5 to 2. Notably, the maximum tensile stress is 89.12 MPa at the shape ratio of 2, which is close to the yield strength of cast iron. This suggests that the current CIPP liner is close to its rehabilitation capacity, and a thicker and stronger liner is required.

Task 4.1 Development of Embedded Distributed Fiber Optic Sensors for Self-sensing Structural Liner (93%), and **Task 4.2** Investigating the Load Transfer between Layers of the CIPP Liner and the Cast-iron

Substrate (78%): During this reporting period, the research team (Dr. Ying Huang and Dr. Xingyu Wang) continued experimental investigations of the smart-liner system under impact loading. To address the limitations of DFOS alone with low sampling rate, a hybrid sensing system combining both fiber Bragg grating (FBG) and distributed fiber optic sensors (DFOS) was implemented. The key findings are summarized below:

(1) Hybrid sensor system: This study presents an innovative smart-liner system that integrates a dual-sensor network for real-time structural health monitoring and deformation visualization. The system captures strain data under both static and impact loading conditions using a combination of distributed fiber optic sensing (DFOS) and fiber Bragg grating (FBG) technologies. As shown in Figure 9(a), the liner is embedded with DFOS along its surface, and an FBG sensor is positioned near the center, adjacent to the DFOS path, to provide complementary high-frequency strain measurements. While DFOS offers continuous spatial sensing, its ability to resolve high-frequency responses is limited due to lower sampling rates. Figure 9(b) compares the strain responses captured by DFOS and FBG under dynamic loading. DFOS effectively tracks strain during the steady and residual phases, showing good agreement with FBG data. However, during initial impact and high-frequency oscillations, DFOS underrepresents peak amplitudes and fails to capture finer oscillation patterns, resulting from its lower temporal resolution. In the developed dual-sensor network, DFOS provides full-field strain distribution for digital twin-based deformation visualization, while FBG enhances temporal resolution for detecting high-frequency events. This integrated sensing approach forms the foundation of the smart-liner system, significantly improving monitoring performance under both static and dynamic loading conditions.

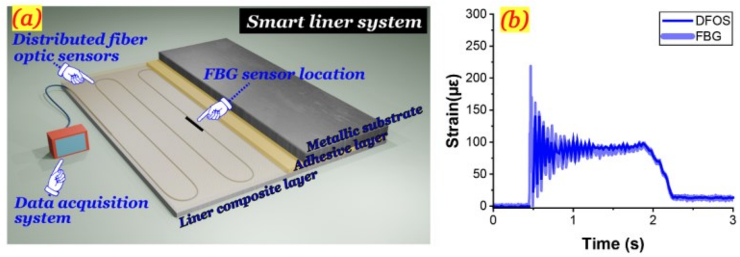

Figure 9. (a) Illustration of the smart-liner system, (b) DFOS and FBG strain signals under dynamic loading.

(2) Impact monitoring and digital twin-based visualization: Using the established FBG sampling frequency, which determines the number of samples collected per second to accurately capture the dynamic response, the strain field can be reconstructed through the dual-sensor network that combines DFOS and FBG. Figure 10 presents the results for the impact at Point #1. The blue line represents strain data obtained from DFOS alone, while the red line reflects the output from the integrated dual-sensor approach. The blue box highlights the limited data coverage provided by DFOS, showing that while DFOS captures part of the dynamic response, it lacks the resolution needed for a complete representation. In contrast, the dual-sensor network offers a more continuous and accurate depiction of the strain response, transitioning from discrete data points to a smoother

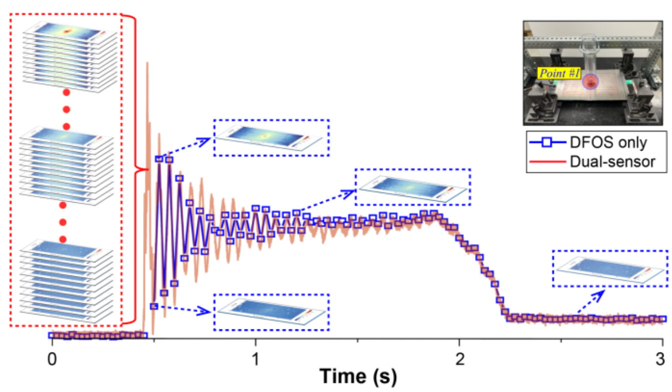

Figure 10. Strain fields after integration of the dual-sensor approach, compared with DFOS only.

and more complete strain field. This integration enables enhanced deformation visualization under impact loading.

Task 5.1 Development of CIPP Liner Risk Index for the Pipeline Integrity Management Enhanced by AI Algorithms (75%): During this period, the research team (Dr. Chengcheng Tao and Huaixiao Yan, Ph.D. student from Purdue University) continued the risk assessment activities using datasets generated from fiber optic sensors under Task 4. A crack identification method was developed, along with a strain field correlation approach to link experimental results with finite element analysis (FEA). Key findings are summarized below:

(1) Crack identification using the dataset from distributed fiber optic sensors: As introduced in the 7th quarterly report, we employed distributed fiber optic sensors (DFOS) to monitor the strain response of CIPP liner under buckling load. Figure 11(a) depicts the strain field at the buckling displacement of 5 mm, obtained by interpolation of DFOS data. When plotting the strain field, we noticed that strain rate changes sharply at some locations, which caused by damages under large buckling deformation. Therefore, we conducted damage identification by localizing the high gradient locations based on strain data collected from DFOS. Figure 11(b) shows the distribution of the strain gradient, areas inside the black contours are potentially damaged regions.

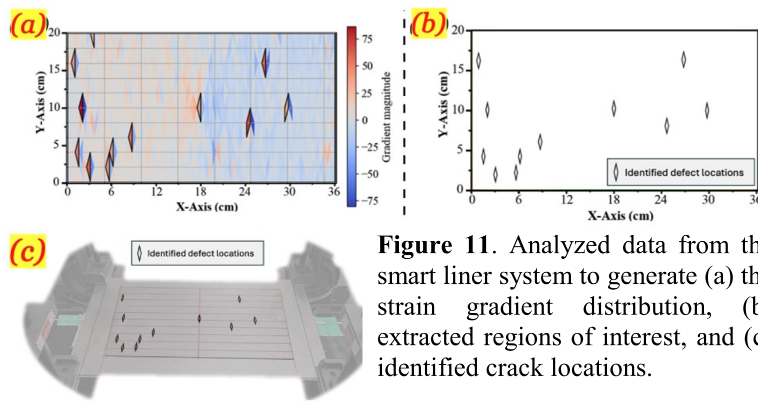

Figure 11. Analyzed data from the smart liner system to generate (a) the strain gradient distribution, (b) extracted regions of interest, and (c) identified crack locations.

(2) Strain field correlation between sensor and FEA results: In the last quarterly report, the experimental and finite element studies on smart liner under impact loading were presented. However, a common issue of experiment and simulation is finding the correlation between them. In this research, an image correlation method is proposed to find the best match between sensor and finite element analysis results. The schematic of the proposed strain correlation method is shown in Figure 12(a). The strain field images from sensor and FEA are input into the neural network to generate their one-dimensional features. To enhance the generation performance, the pre-trained neural network model, ResNet18, is used. The final correlation is performed using cosine similarity, which reduces the influence of feature length on the matching process and improves computational efficiency. Figure 12(b) shows the results of the strain field correlation method, and according to the results, the strain field correlation method achieves great accuracy.

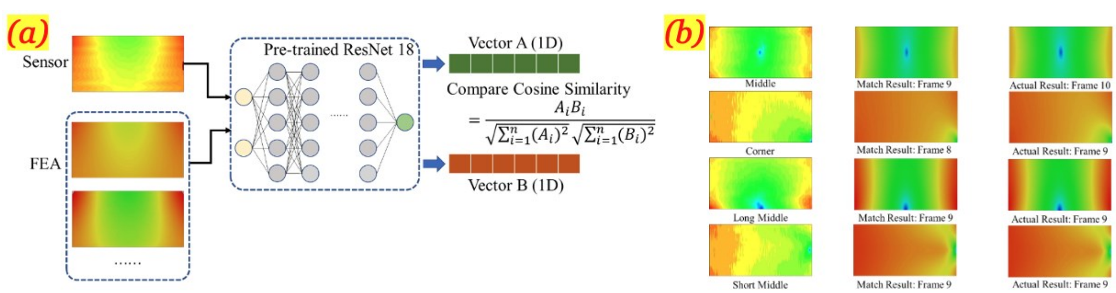

Figure 12. (a) The schematic of strain field correlation; (b) Strain field correlation results

Project Financial Activities Incurred during the Reporting Period:

The cost breakdown during the reporting period according to the budget proposal is shown in Table 2.

Table 2. Cost breakdown

Category	Amount spent during Q11
Personnel	
Faculty	$0.00
Postdoc	$1,499.91
Students (RA and UR)	$16,634.63
Benefits	$884.06
Operating Expenses	
Travel	$0.00
Materials and Supplies	$516.75
Recharge Center Fee	$3,551.00
Consultant Fee	$1,500.00
Subcontracts	$29,780.24
Indirect Costs	$11,063.89

Project Activities with Cost Share Partners:

The Match fund from NDSU for this project is coming from the tuition of the associated graduate students during their work on this project. During the reporting period (Q11), Zahoor Hussain (100%), Muhammad Imran Khan (100%), Austin Knight (100%), and Tofatun Jannet (46.15%) were working on the project. The tuition for the four students during Q11 was estimated to be $12,520 at a rate of $463.73 per credit.

Project Activities with External Partners:

During this reporting period, George Ragula, our industry consultant, attended all the bi-weekly meetings with the research team.

Potential Project Risks:

No potential risks were noticed during this reporting period.

Future Project Work:

The research team will continue working on Tasks 2, 3, 4, and 5.

Potential Impacts on Pipeline Safety:

Continuing from Q10, a new self-healing polymer formulation was developed using an acrylate reactive diluent that contained sufficient diacrylate impurities. This approach addressed the undesirable melting behavior typically seen in homopolymers and resulted in improved thermal performance. For the vitrimer system, molecular dynamics simulations were conducted to comprehensively evaluate the previously developed model, with a focus on glass transition temperature, porosity, and mechanical properties. In parallel, a hybrid sensing system combining FBG and DFOS was implemented in the smart-liner system to capture more detailed responses under impact loading. FEA modeling and risk analysis were closely integrated with the experimental data collected from the smart-liner system, enabling more accurate structural assessment and deformation visualization. These findings provide a deeper understanding of the developed all-in-one smart-liner system and demonstrate its enhanced performance. The results highlight its potential to improve reliability and support failure prevention, offering valuable insights for optimizing the design and manufacturing of CIPP liner systems.